Research Article

Paper presented in the special issue of [Advanced Materials in Additive Manufacturing]

Structural Condition Monitoring Using Deep Learning on a Metallic Part Fabricated by Additive Manufacturing

Romaine Byfield[ID]**, Ghani Semroud**[ID]**, Matthew Laurent**[*]**, Ibrahim Tansel**[ID]

Department of Mechanical and Materials Engineering, Florida International University, Miami, Florida, USA
E-mail: mlaur034@fiu.edu

Abstract: Additive manufacturing (AM) was originally developed to manufacture polymer prototypes. Today, it has been used for the manufacturing of many critical machine components. Most of the structural health monitoring (SHM) methods were developed for monitoring the condition of large and thin plates on airplane fuselages. Additively manufactured parts are generally small, thick, and have complex geometries. SHM methods have been improved to sense load, detect defects, and identify loose bolts with the help of a permanently installed sensor. In this study, the adaptability of SHM methods was researched with additively manufactured metal parts with complex geometry. Magnets were used to apply pressure to 9 different locations on the surface of a stainless steel additively manufactured thick plate with deep groves. SHM was used to estimate the magnets' location. Many SHM (Lamb wave) methods cannot work on smaller parts since their dimensions are shorter or very close to the wavelength of the created oscillations. Surface response to excitation (SuRE) method which has similar characteristics to electromechanical impedance methods was used for data collection. To obtain descriptive features of the time domain data, fast Fourier transformation (FFT), short-time Fourier transformation (STFT), continuous wavelet transformation (CWT), and synchrosqueezing transform (SST) were applied to CWT. 1D and 2D convolutional neural networks (CNN) were used to classify the cases. When CNN was optimized for the analysis of our data, 100% location estimation accuracy was obtained by using 50% of 320 scalograms for training. The scalograms were obtained by enhancing the CWT results with SST. STFT-CNN combination was the second best. It obtained 95% accuracy with the same number of spectrograms and training allocation.

Keywords: SHM, AM, data processing techniques

Nomenclature

x_n/x The given signal in the time domain in the STFT function
w_n The analysis window function
m The time index of the STFT function
ω The sampling frequency of the STFT function
n The step size
a Dilation/scaling parameter in the CWT function
τ The location of the wavelet of the CWT function

ψ	The wavelet function, a mathematical function used in digital image processing and compression to improve image quality
t	Time
T	A parameter of waves, the period is a definite interval between two points in time

1. Introduction

Additive manufacturing (AM) emerged in the 1980s as a pioneering technique for producing polymer prototypes, and over time, there has been a notable advancement in the quality, quantity, and diversity of materials used in additively manufactured parts. Additively manufactured products have found applications across a wide range of industries, spanning from soft polymer parts [1] to highly durable aerospace components [1]. With critical applications, it will be necessary to evaluate loads in order to detect loose bolts and identify flaws. Structural health monitoring (SHM) [2, 3] methods have been developed for these types of applications and optimized for many metal structures such as the plates of the fuselages seen in airplanes and wind turbine blades. The evaluation of polymer or metal additively manufactured parts using existing SHM methods is ineffective, requiring modifications that account for the unique geometry and properties of these parts. This study aims to assess the applicability of the surface response to excitation (SuRE) method for SHM in such scenarios. By attaching a magnet to various positions on a complex stainless steel additively manufactured part, a distributed load was applied to a small area of the plate, allowing for the evaluation of SuRE performance without causing damage to the workpiece. The investigation focused on determining the accuracy of surface load location estimation achieved through the SuRE method.

In recent research studies, SHM methods typically comprise three main components. The first component involves the collection of experimental data, where measurements are gathered to capture the behavior of the structure or component under investigation. The second component focuses on processing the collected data to aid/ facilitate the subsequent classification and analysis of the data. The third component entails the classification of the processed data, where algorithms or techniques are employed to categorize the data into different classes or states. This classification process enables the identification and assessment of the condition or performance of the structure or component being monitored.

In aerospace and mechanical engineering applications Lamb wave (LW), electromechanical impedance (EMI), time reversal (TR), and heterodyne effect (HE) are the most used procedures for data collection. The LW method [4, 5] uses one or multiple piezoelectric elements for excitation and data collection. The location of the defect can be estimated with good accuracy by tracing the wave propagation. The EMI method [6-8] uses one or more piezoelectric elements and evaluates the change of the EMI characteristics by using an EMI analyzer. SuRE method [9, 10] has similar characteristics to the EMI. However, there is no need for an EMI analyzer. In addition, any exciter and sensor may be used for data collection if they have proper frequency response and characteristics [11]. LW and EMI methods need a reference to compare the signal. TR and HE methods monitor the characteristics of the structure between the piezoelectric elements to determine if it is linear or nonlinear. These methods don't need to compare the signals with a reference. A well-made solid structure and tightened joints have the characteristics of a linear system. If a defect develops, the structure becomes a nonlinear system. TR method [12] sends a harmonic signal from the exciter to the sensor. The sensor sends the received signal back to the exciter after it is properly processed. The received signal at the exciter is very similar to the original signal if the structure is in perfect condition. Defects create nonlinearity, hence sent and received signals will have different characteristics. The HE method [13, 14] sends the addition of two harmonic signals from the exciter. If the structure is in perfect condition and the bolts are tight, the sensor sees the signal with the excitation frequencies. In the case where there are loose bolts or disbanding between the layers, the system becomes nonlinear, and a new harmonic signal develops at the difference of the frequencies of the transmitted signals. LW methods are expected not to work effectively with small parts that have dimensions smaller than the wavelength of the excitation signal. Since the magnet did not affect the linearity of the part, the SuRE method was selected and used in this study.

Fourier transformation (FT), short-time Fourier transformation (STFT), and wavelet transformations have been widely used for signal processing in SHM applications to extract the characteristics of the signal in a more compact and representative way. FT [15] was used in many studies to obtain the spectral characteristics of the signals in the

frequency domain [16]. However, it is difficult to encode 1D amplitudes of the spectrums to train conventional neural networks. Recently, time-frequency methods such as STFT [17] and wavelet transformation (WT) [18] have been used since many deep learning neural networks were developed to classify 2D images automatically. STFT has constant frequency resolution, hence the user needs to compromise either the time or frequency domain resolution. WT has better computational efficiency. Since the frequency resolution widens at the higher frequencies.

For classification of the processed SHM data, comparison of the spectrum, artificial neural networks (ANNs), support vector machines (SVMs), k-nearest neighbors (KNNs), and deep learning have been widely used. For the quantitative representation of the frequency domain results, the sum of the squares of the spectral differences (SSD) of the spectrums [19] or similar statistical parameters [20] such as root mean square deviation (RMSD), and the means absolute percentage deviation (MAPD) were used. Instead of writing programs, multipurpose ANN [21] software is capable of learning the characteristics of the signals and classifying the given cases after training [22, 23]. The user must determine the most descriptive features and encode the data for ANNs. Since the spectrum obtained by the fast Fourier transformation (FFT) of SHM data is generally very complex for encoding, other parameters such as strains have been preferred [24]. SVM [25] can generalize the shorter datasets better compared to the ANNs and may deal with larger numbers of features [26, 27]. KNN algorithms [28] have been developed from a simple and very efficient nearest neighbor pattern classification (NNPC) method [29] as it performs favorably in many studies [30]. Deep learning convolutional neural network (CNN) [31] is capable of classifying 2D images without any encoding. Time-frequency plots of STFT and WT [32] or square matrices created with Euclidian distances [33] may be used to generate 2D images to work with the CNN.

Additive manufacturing methods build parts layer by layer, allowing for precise control and customization of the final product. The first commonly used machines created polymer parts by curing the liquid resin with a laser [34] or melting a filament [35] selectively. Selective laser sintering (SLS) [36] and selective laser melting (SLM) [37] equipment was developed later to build the metal parts in a metal powder bed. Metal fused filament fabrication (MFFF) methods [38] of Markforged and desktop metal create the part layers by melting a rod or a filament made of metal powder and polymer (binder). After the washing and sintering process, a fully formed metal part with the desired geometry is achieved. Recently, wire arc additive manufacturing (WAAM) has been gaining popularity in manufacturing large-size parts with limited dimensional resolution [39, 40]. Additive manufacturing has found many applications in industry and it will continue to increase its gains in the future [41-43].

The work focuses on polymer parts with varying internal geometries (infills) to study and improve the ability of the SuRE method [44] when they were used to estimate the load location, infill density, and artificial corrosion and cracks. It was discovered that small polymer parts attenuated the surface waves quickly. In this study, additively manufactured metal parts were used, and the challenge was to obtain meaningful data while the created waves moved along the surface with very little attenuation relative to polymer parts. Continuous wavelet transformation (CWT) signals were enhanced with synchrosqueezing transform (SST) and classified using the CNN.

The paper attempts to explore an original approach to evaluating the effectiveness of SHM methods on an additively manufactured part with complex geometry. The goal is to figure out the crucial factors for accurate defect identification as well as find the correct optimization that can be used for future SHM methods and other data-processing techniques that are discussed at length throughout the rest of this paper. The purpose of this work is to consider the limitations and boundaries of the techniques used in SHM methods, formulate the key requirements for optimal results, and present the promising potential in additively manufactured parts.

2. Theoretical background of signal/data processing techniques

The classification of wave propagation is easier in the frequency domain compared to working in the time domain is easier since the frequency domain shows much of a signal lies within each given frequency band over a range of frequencies [45]. There are many different tools available to convert data from the time domain to the frequency domain, each with its own advantages and disadvantages [46, 47]. Two techniques that are widely used for data processing in SHM are the STFT and the WT. The STFT is used to observe wave propagation, separate the reflected waves from the incident waves, and designate the associated damage measures [48, 49]. The WT is very effective for denoising and feature extraction [50]. The frequency resolution of the STFT is fixed and very detailed signal analysis can be done

by overlapping the analysis windows at the expense of the computation time. Time and frequency resolutions need to be compromised according to window length. Time and frequency resolutions are inherently adjusted at WT and computations are extremely efficient. However, the frequency resolution of the WT changes at different frequencies.

2.1 STFT

The STFT is calculated by dividing the signal into consecutive segments of what we will refer to as windows. The spectrogram is created by calculating the Fourier spectrum of each window one by one [51] filling results along the columns of a 2D matrix and repeating the process for consecutive windows. STFT is usually visualized using its spectrogram, which is an intensity plot of the magnitude of the STFT against time [52-54]. The spectrogram is prepared from this matrix with time in the x-axis and frequency in the y-axis, and the amplitude/power of the signal is represented by the color or gray level according to the magnitude of the element. The length of each segment/epoch is determined by the window size. STFT provides the time-localized frequency information for situations in which frequency components of a signal vary over time, compared to the standard Fourier transform provides the frequency information averaged over the entire signal time interval [55]. One drawback of the STFT is that there is a trade-off between time and frequency resolution. Short window length results in a better (finer) resolution in the time domain, it generates a poor (coarser) resolution in the frequency domain, and vice versa.

The equation for the STFT is shown in equation (1), where x_n is the input signal, w_n is the window function, m is the time index, ω is the frequency and n is the step size.

$$\text{STFT} = X(m,\omega) = \sum_{n=-\infty}^{n=\infty} x_n w_{n-m} e^{-i\omega t_n} \tag{1}$$

2.2 WT

The WT is a tool that separates the signal/data into different signal components, with each having a resolution that matches its scale [56, 57]. In other words, the WT has the capability to use several time resolutions, in contrast to windowed Fourier transforms, where a fixed window size is used for all frequency components [58]. Taha et al. [59] mentioned that it is important to note that WT should not be considered as competition to the FT but as an extension of this technique.

2.3 CWT

CWT has been gaining popularity. The CWT maps the original time series, which is only a function of time, into a function that contains two variables: time and frequency. Computations take time to create the redundant information [60]. However, this redundancy makes it easier to analyze and classify the data compared to other forms, such as the discrete wavelet transform (DWT) [61-63]. CWT can be calculated with the following equation (2) from a given signal.

$$\text{CWT}(a,\tau) = \frac{1}{\sqrt{a}} \int_{-\infty}^{\infty} x(t)\psi\left(\frac{t-\tau}{a}\right)dt \tag{2}$$

where a is the dilation/scaling parameter, τ is the location of the wavelet, ψ is the wavelet function and x is the signal.

The SST was applied to the CWT, to assess its impact on the CNN's ability to extract the features from the signal. The purpose of the SST is to sharpen linear time-frequency representations (TFRs), like the CWT. It is built on an estimation of the instantaneous frequency (IF) of each mode from the TFR. This is used to sharpen and squeeze the energy of the representation [64-66]. In order to create an image with sharper rendering.

2.4 CNN

CNNs similar to traditional ANNs incorporate neurons that self-optimize through learning. As seen in traditional ANNs, each neuron will still receive an input and perform an operation [67]. In other words, they consist of neurons and use weights that change in each iteration (forward and backward pass of a set of data through the network) to simulate

the learning process. What sets them apart is that CNNs, as the name suggests, consist of convolutional layers. These layers contain filters that are passed through with the input image to create a feature map. CNNs are primarily used in the field of pattern recognition within images.

2.5 *Windowing*

There are many different types of windowing functions available. Two commonly used windows are the Hann and the Hamming windows. These window functions are useful with better frequency resolution compared to other windows, but moderate side lobes do not present a problem. The Hann and Hamming windows differ in the way they taper at the ends, where the Hamming window doesn't reach zero (0.8), hence still has a small discontinuity in the signal. Due to this difference, the Hamming window does a better job of canceling the nearest side lobe [68]. Equation (3) is used to calculate the coefficients of the Hamming window [68].

$$w_n(t) = 0.54 - 0.46 \times \cos(2\pi t / T) \tag{3}$$

In most applications, any one of the windows considered above, except the rectangular window, will give acceptable results. The Hamming window is preferred by many due to its relatively narrow main lobe width and good attenuation of the first few side lobes [69].

3. Experimental setup

The diagram and picture of the experimental setup are presented in Figures 1 and 2 respectively. An additively manufactured stainless steel test plate (17-4 PH Stainless Steel v1) was used in the study (Figure 3) with exact specifications shown in Figure 4. The test plate was 225 mm long and 75 mm wide. It was printed by using a Mark forged Metal X 3D printer. The part was built with 1 mm height layers with 100% infill. It had rectangular slots. Each slot was 1.83 mm wide. There was a 6.38 mm gap between the slots. The slots had three depths: shallow (3.10 mm), medium (5.00 mm) and deep (7.15 mm).

Two piezoelectric transducers (Steminc SMD12T06R412WL) were bonded to the opposite sides of the plate with a 195 mm distance (Figure 3). M-Bond 200 adhesive was used to attach the disks. Rigol DG1022Z function/arbitrary waveform generator was used to excite the piezoelectric disk on one side of the test plate. An OWON XDS3104AE digital oscilloscope was connected to the piezoelectric disk on the other side of the plate to acquire the data. The function generator excited the disk with a sweep sine wave ranging from 100 to 120 kHz with a p-p amplitude of 20 V.

Reference data was collected first without attaching any magnets to the plate. Later, three magnets were put on top of each other. Each magnet had a holding force of 16 lbf on the steel plate. Data was collected by attaching the magnets to 9 different locations on the test plate to collect the experimental data. At each test, three magnets stayed on top of each other. The location of the magnets is presented in Figure 5. The distance between the selected magnet locations was 65 mm horizontally and 25 mm in the vertical directions.
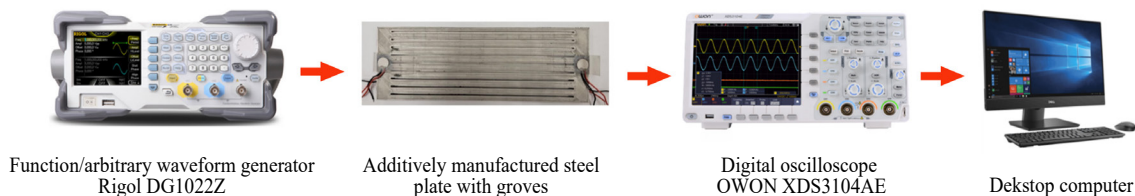

Function/arbitrary waveform generator
Rigol DG1022Z

Additively manufactured steel
plate with groves

Digital oscilloscope
OWON XDS3104AE

Dekstop computer

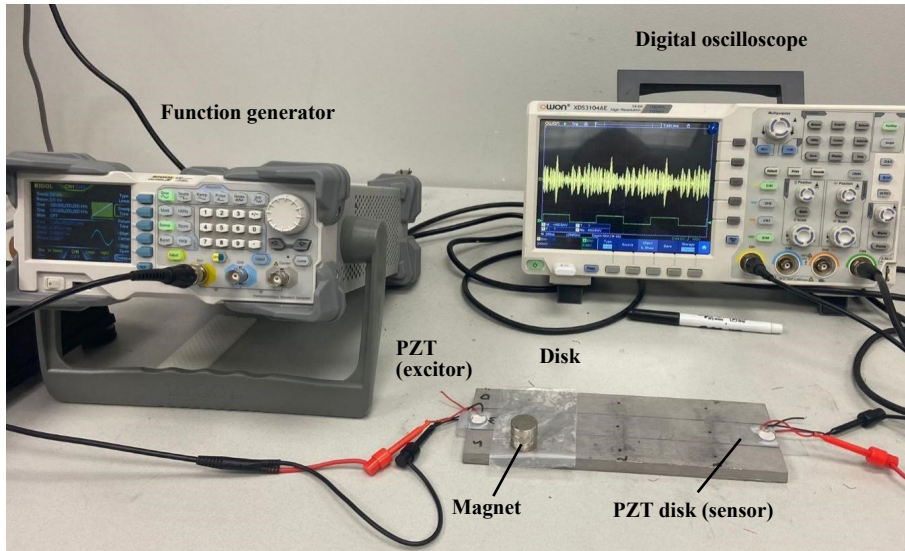**Figure 1**. The diagram of the experimental setup

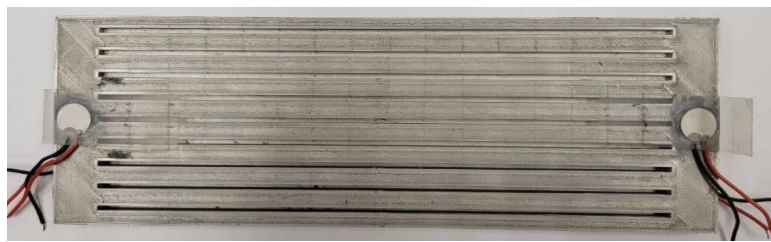**Figure 2**. Picture of the experimental setup

Figure 3. Picture of the additively manufactured stainless-steel test plate
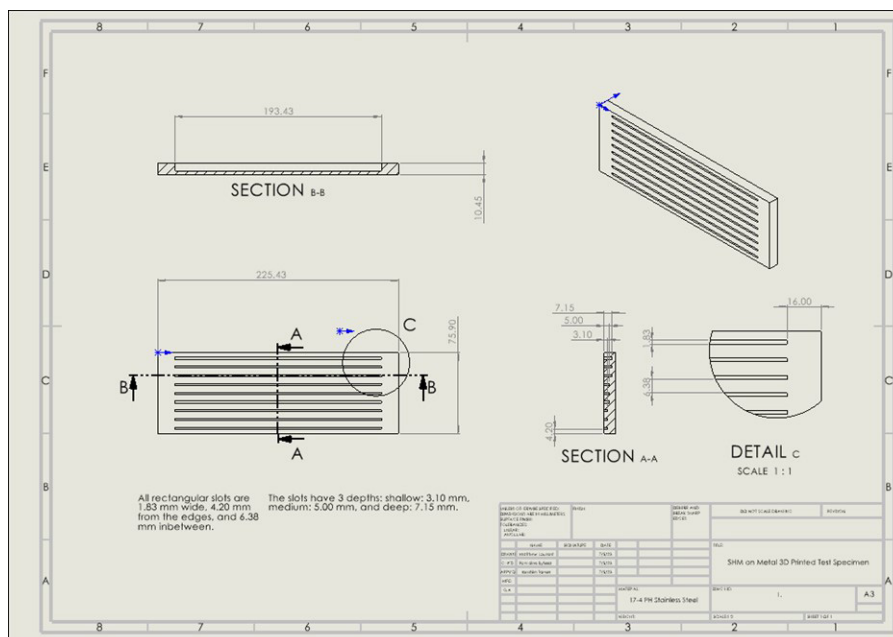

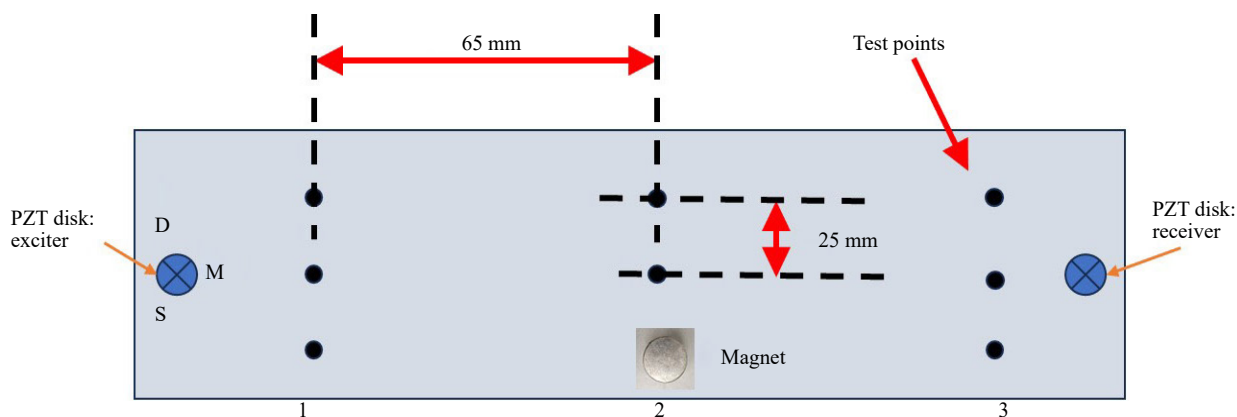**Figure 4.** Dimensions of the stainless-steel test plate

Figure 5. Test points of the magnet (three different points longitudinally with a spacing of 65 mm and three different points laterally with a spacing of 25 mm, totaling nine different points)

4. Data analysis and classification

Two experiments were performed 320 times in the study: one without any magnets and two when the magnets were placed in 9 different locations. For the first half of the study, only 25% of the dataset was used then in the later half all 320 datasets were used. For all data, FFT, STFT, and CWT were calculated. For classification, 1D and 2D CNN were used in the study. The data processing techniques and classification method combinations are outlined in Figure 6. The 1D spectrum of the FFT was used to train and test the 1D CNN. 2D time-frequency spectrogram of STFT and scalograms of CWT were used to train and test the 2D CNN. In addition, scalograms were enhanced by using SST with CWT in order to train and test the 2D CNN. The initial and final versions of the 2D CNN architectures are presented in Figures 7 and 8 respectively with the convergence plot for the CNN architecture shown in Figure 9. The architecture of the CNN was changed to improve the performance of the algorithm until 100% estimation accuracy was obtained. To find the optimal architecture, CNN was tested many times with different combinations of convolution layers, pooling layers, and other components.
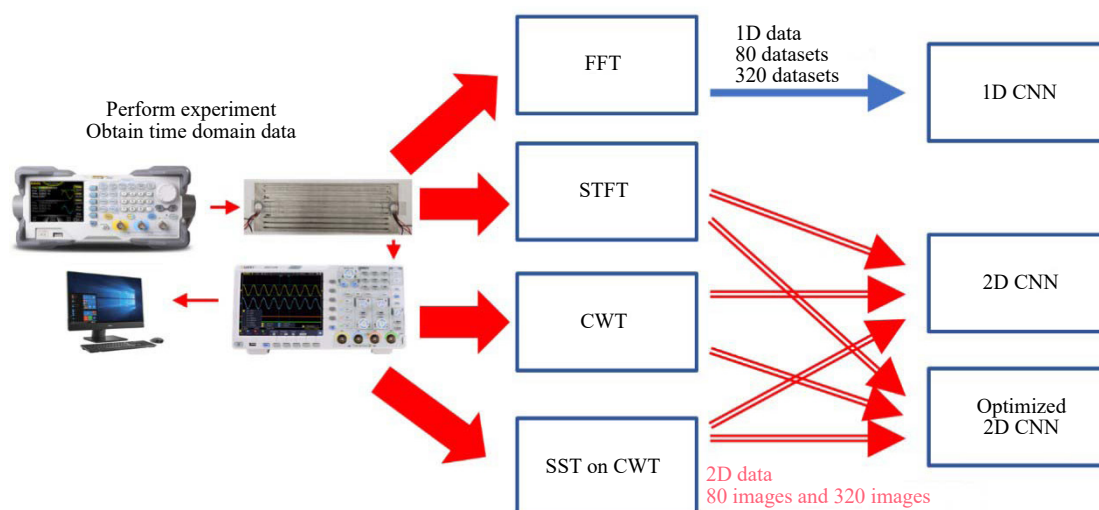

Figure 6. Flow chart showing the data gathering, processing, and classification steps
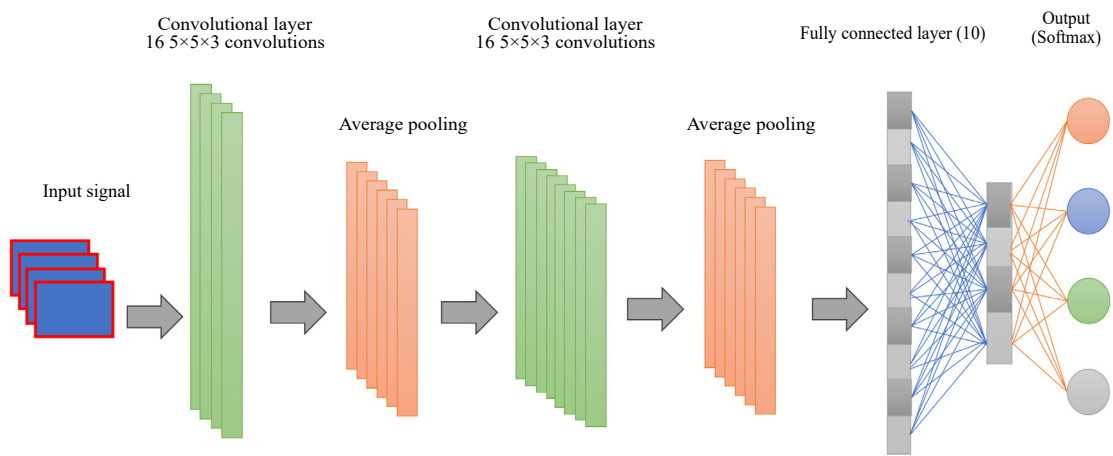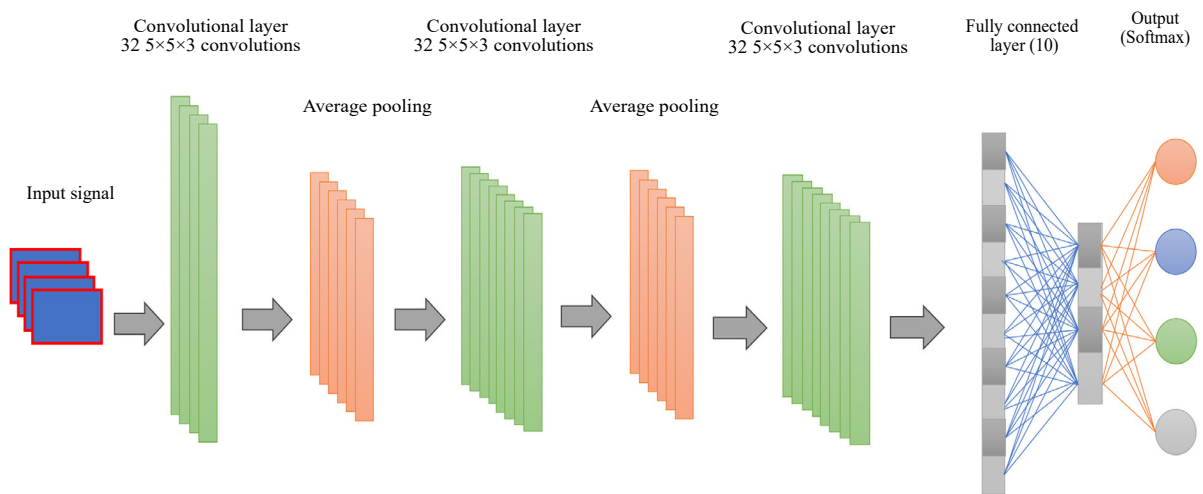
Figure 7. Initial 2D CNN algorithm

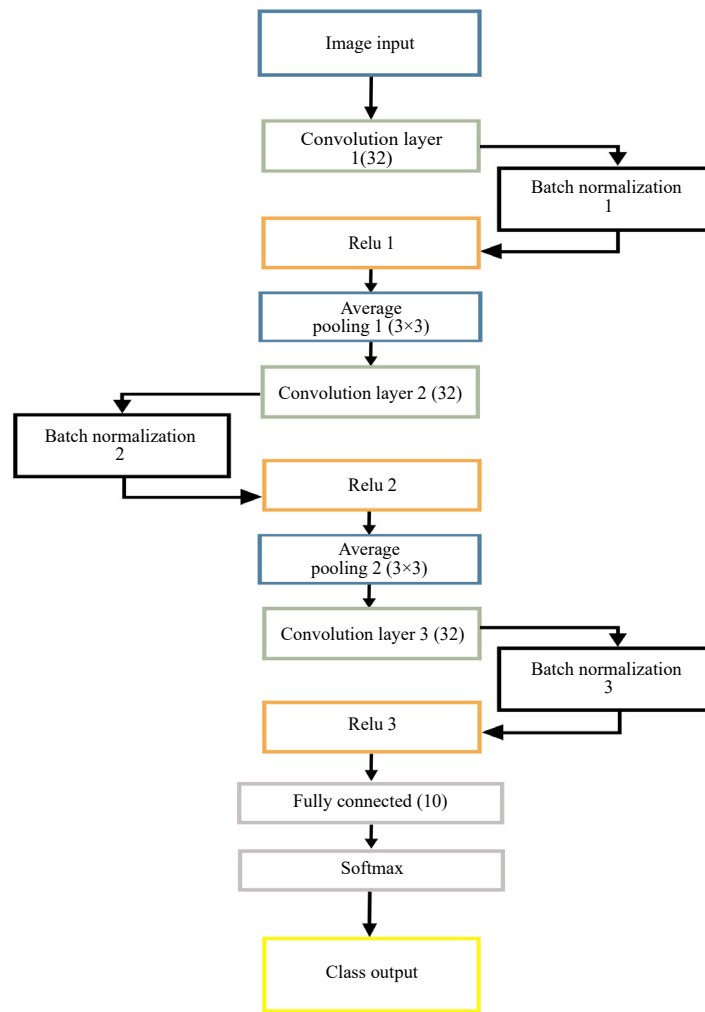**Figure 8**. Optimized 2D CNN algorithm

Figure 9. Additional convergence plot for optimized 2D CNN architecture

5. Results

The results will be presented in 4 sections. First, the time and frequency domain characteristics of the collected data will be evaluated. Second, the spectrogram of STFT, scalogram of CWT, and SST enhancement of the CWT will be discussed. Third, performances of 1D CNN working with FFT, 2D CNN working with STFT, 2D CNN working with CWT, and 2D CNN working with SST-enhanced CWT will be compared. Fourth, the architecture of the 2D CNN working with SST will be optimized. The performance of the optimized 2D CNN (O-2D CNN) will be evaluated with all the processing methods and the best training data set size will be determined for the best performing approach.

5.1 *Time and frequency domain characteristics of the collected experimental data*

The time domain data presented in Figure 10 serves as a baseline for when there is no magnet on the plate. The time domain data when the magnet was put at 9 different test points on the plate are presented in Figure 11. These figures clearly demonstrate an overall decrease in the amplitude of the signal received at the sensor when the magnet was attached to the test locations with the most significant changes being the profile of the envelope, while the general shape remained relatively consistent.

Looking at Figure 11 and comparing it to both Figures 10 and 12, the plots clearly indicate that the character

the signals were significantly changed when the magnets were attached to different test points creating disparity between almost all testing points.
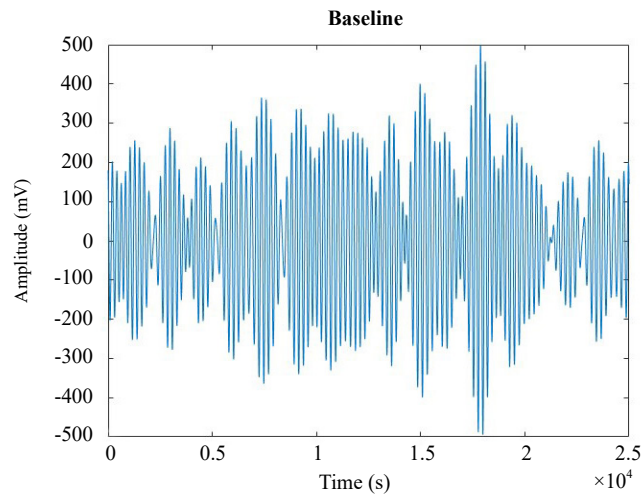

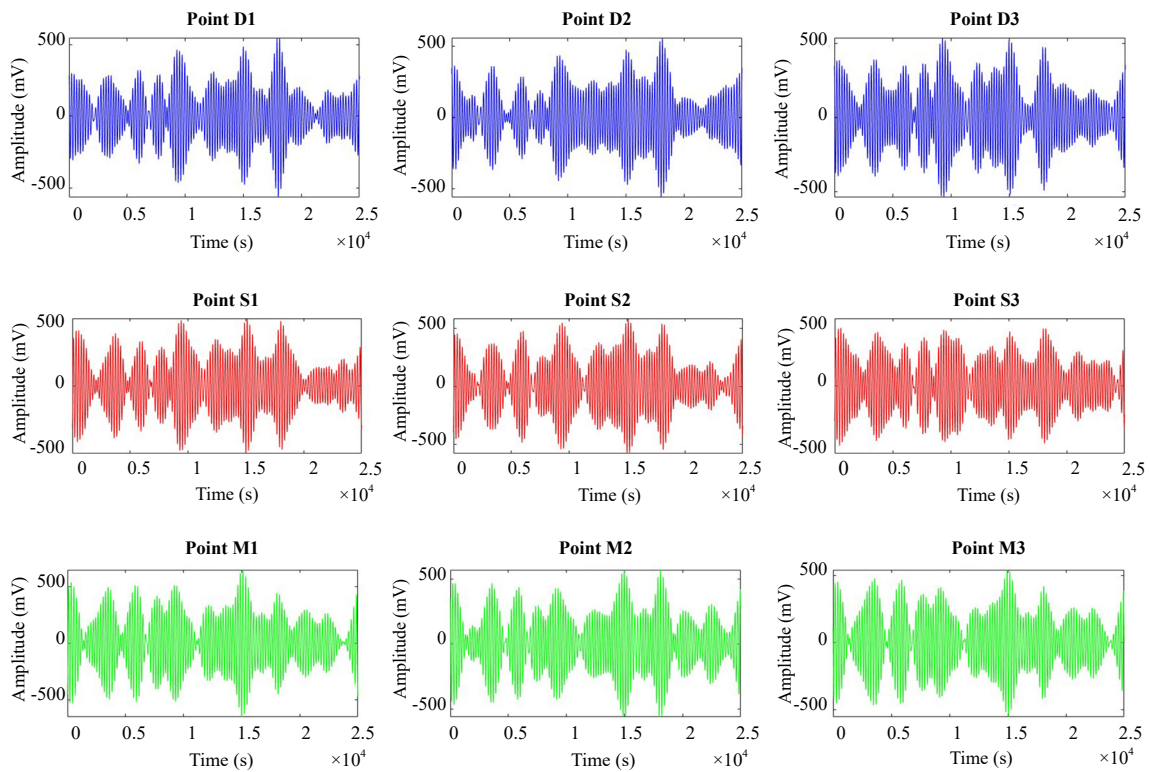**Figure 10**. Time domain response for baseline readings

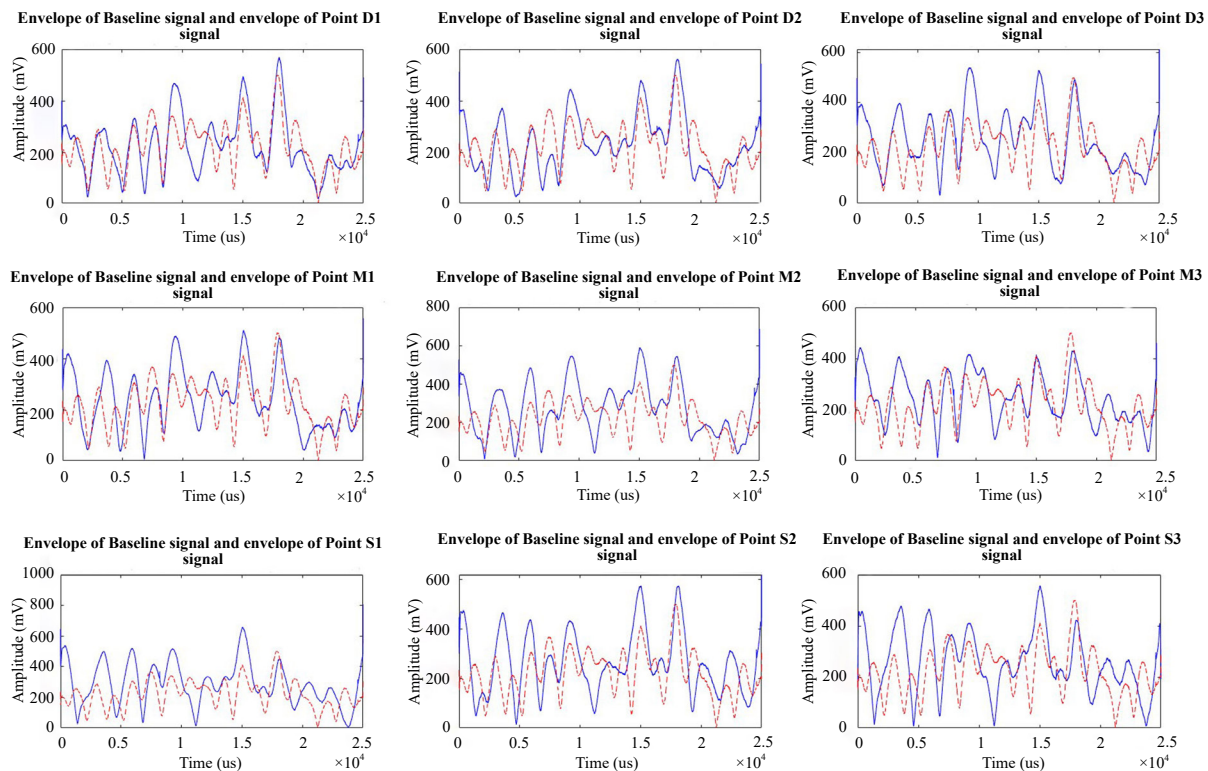**Figure 11.** Time domain response for the magnet placed at each point

Figure 12. The envelopes of the acquired signals when the magnet was attached to the test points (blue line). The envelope of the baseline is presented with red broken lines.

Figure 13 presents the frequency domain plots for each signal and the baseline. Each FFT of the signals obtained at different magnet locations had distinct patterns. To minimize the similarity of the signals when the magnets were attached to the top half and the bottom half the depth of the groves were different. Shallow groves had 3.10 mm depth at the bottom half while the deep groves at the top had 7.15 mm depth. The frequency domain analysis demonstrates clear changes in the profiles of the signals, indicating a correlation between the magnet placement and the characteristics of the FFTs. However, even the 1D FFT is very complex to encode manually in order to work with conventional neural networks which prefer to have less than 10 inputs. These signals were given to 1D CNN for classification.

5.2 *Data process methods including spectrogram, scalogram, and SST enhancement of the scalogram*

The spectrogram created by the STFT of the baseline signal is presented in Figure 14. The scalogram of the same data is presented in Figure 15 after it was calculated by using the CWT. The studied test band around the excitation frequency range is presented in Figure 16. SST was applied to the CWT in Figure 16 and presented in Figure 17. By applying the SST to the CWT, the resulting image in Figure 17 exhibits enhanced localization of peak features, which are crucial for identifying significant patterns and details in the analyzed data. This improved visual representation offers a more distinct and informative image, allowing CNN to potentially extract and leverage these features more effectively during the classification process.

The clearer peaks observed in Figure 17 indicate that the application of the SST to the CWT enhances the representation of salient features within the data. These enhanced features can aid CNN in its ability to distinguish important patterns and make more accurate classifications.

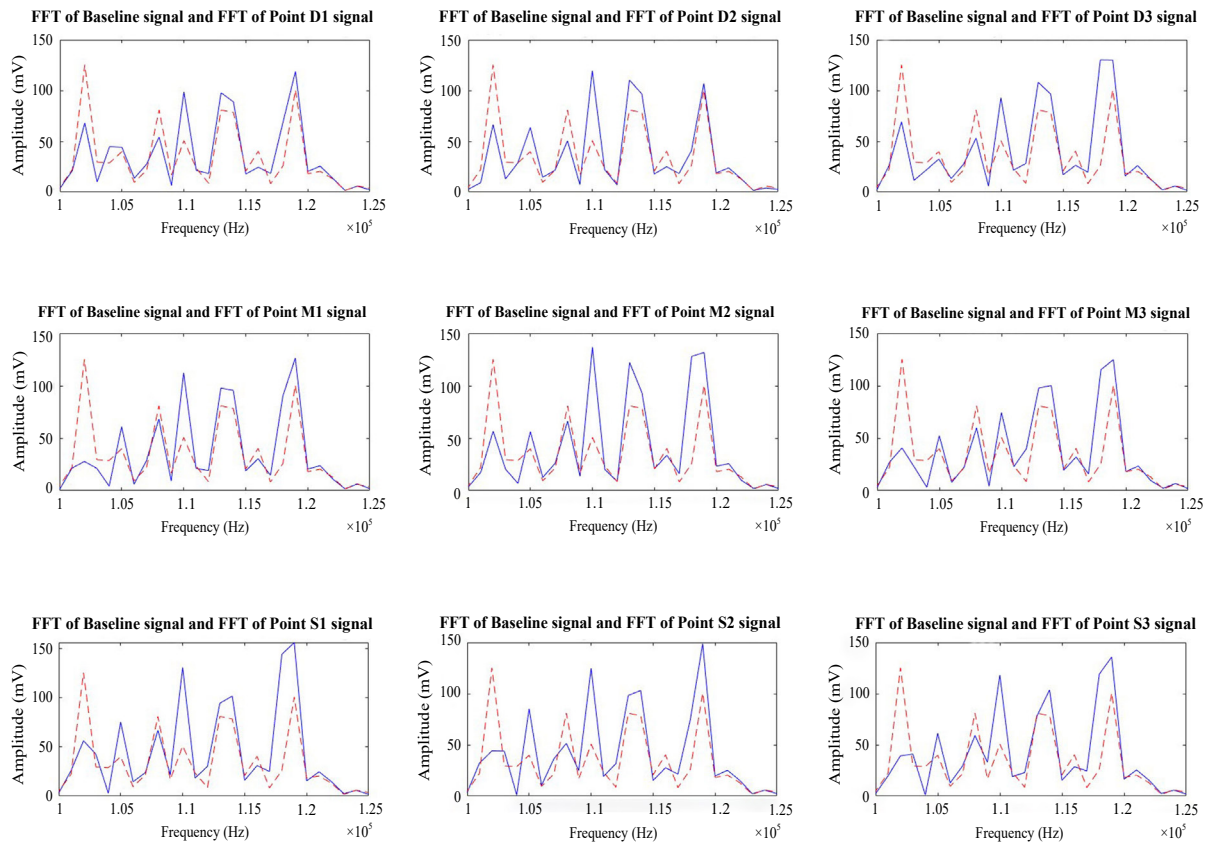**Figure 13.** FFT of the signal when the magnet is attached to different test points (blue line). For comparison, the FFT of the baseline is presented with the red dashed line.
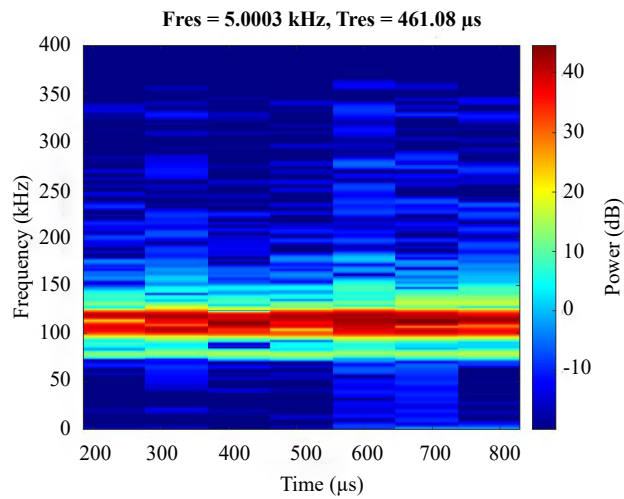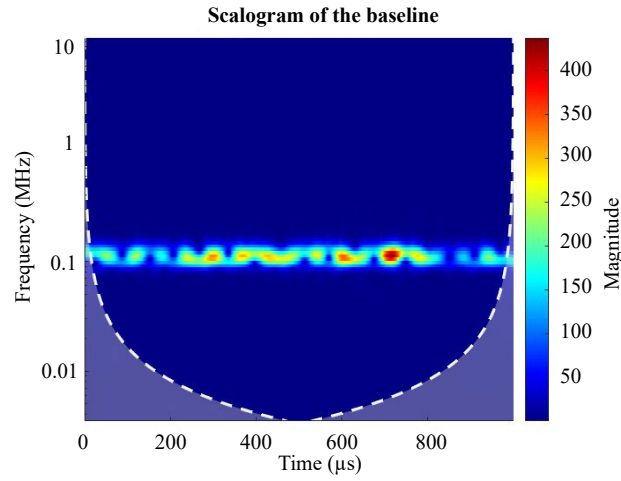

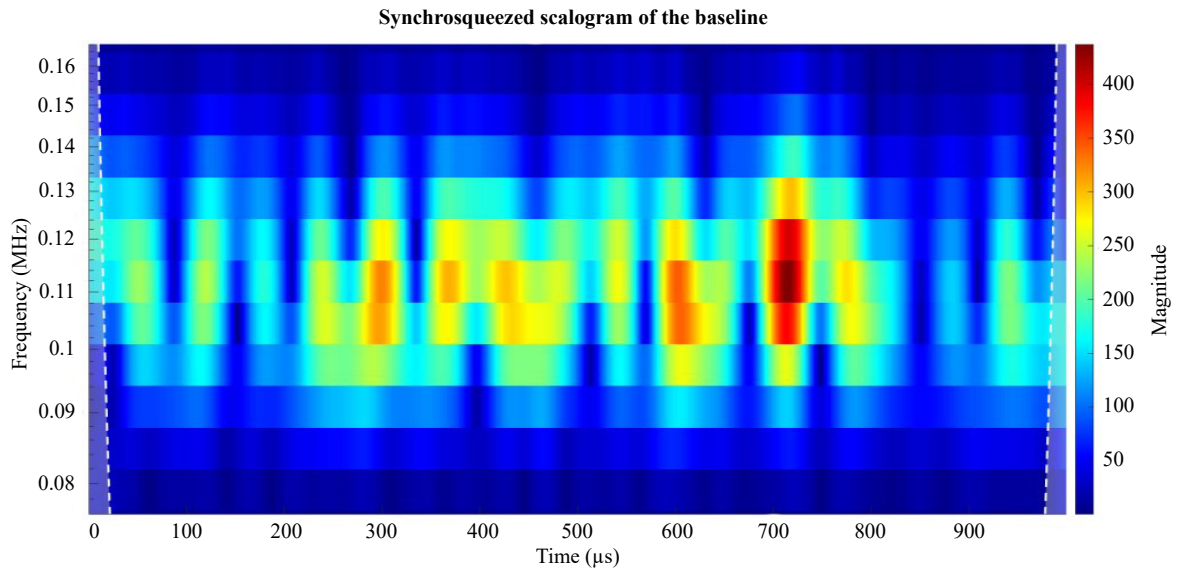**Figure 14.** Spectrogram created using STFT

Scalogram of the baseline

Figure 15. Scalogram created using CWT

Synchrosqueezed scalogram of the baseline

Figure 16. Scalogram created using CWT with reduced frequency range

Synchrosqueezed scalogram of the baseline
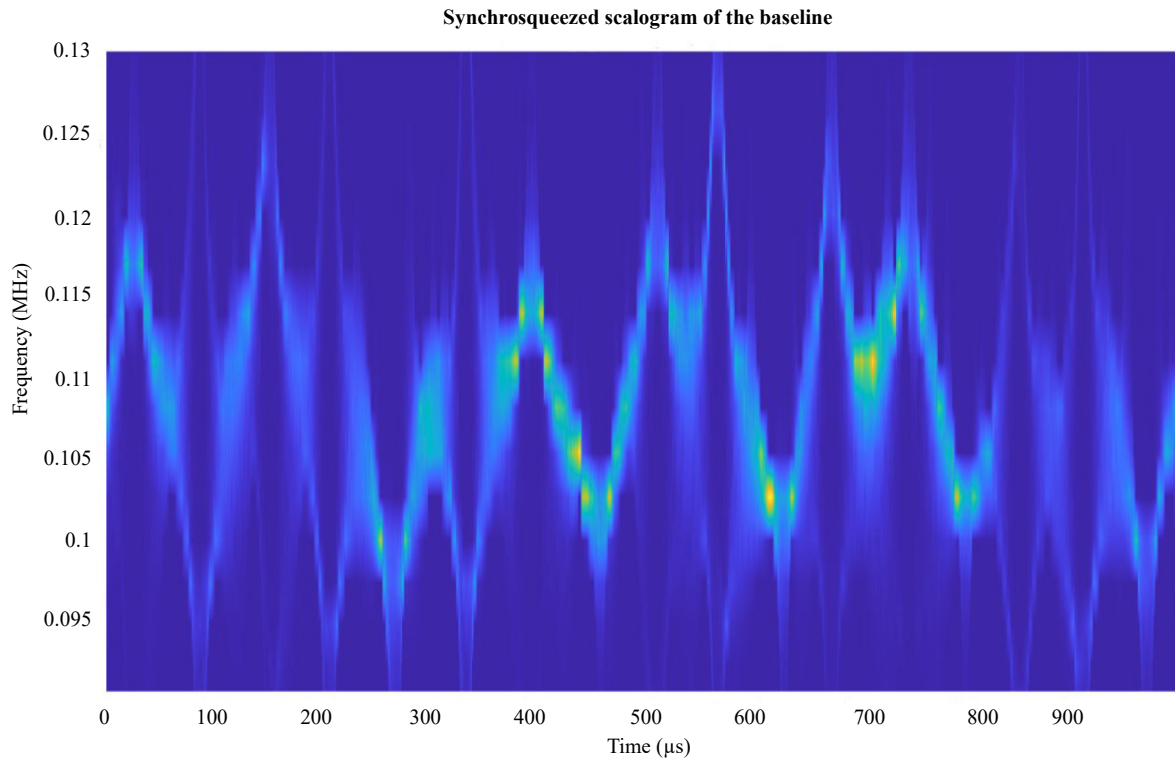
Figure 17. Scalogram created using SST on CWT

5.3 *Comparison of the performances of different data processes and classification combinations*

First, the test data of 80 experiments were used in the study to select the best data processing and classification combination. 1D CNN with FFT spectrums, 2D CNN with spectrograms of STFT, 2D CNN with scalograms of CWT, and 2D CNN with SST-enhanced scalograms of CWT were used. In all these studies the initial architecture of the CNN was used. It was trained with 50% of the data. The confusion matrix in Figure 18 showed that 1D CNN obtained the lowest accuracy of 50% when it was processed with the spectrums of the FFT. 2D CNN obtained the second-best performance with 63% accuracy when the spectrograms of the STFT were used as seen in the confusion matrix in Figure 19. The confusion matrix in Figure 20 displayed that 2D CNN which was trained and tested with the CWT obtained a very low accuracy of 50%. When the SST was used to enhance the scalograms of the CWT, the 2D CNN obtained the best results with 66% accuracy according to the confusion matrix in Figure 21. These results indicated that STFT is computationally very expensive but capable of obtaining great results if the window size is selected properly. 2D CNN-SST enhanced CWT (CWT-SST-2D CNN) was selected as the best combination for the rest of the study. When a sweep sine wave is applied, theoretically FFT-1D CNN and STFT-2D CNN combinations are expected to perform almost the same. However, that wasn't the case. Most likely, because of the reflecting waves, the receiver acquired signals outside of the excitation frequency, potentially providing some useful information. The excitation frequency range was selected very narrow (100 to 120 kHz) in this study to avoid the presence of surface waves with very high or very low frequencies at the same time.

Figure 18 content (Accuracy = 40%):

True class \ Predicted class	BASELINE	D1	D2	D3	M1	M2	M3	S1	S2	S3		
BASELINE	1	1			1						33.3%	66.7%
D1		2				1					66.7%	33.3%
D2			2			1					66.7%	33.3%
D3		1		1		1					33.3%	66.7%
M1			1		1	1					33.3%	66.7%
M2					1	2					66.7%	33.3%
M3					3							100.0%
S1						1		1	1		33.3%	66.7%
S2	1							1	1		33.3%	66.7%
S3	1							1		1	33.3%	66.7%
	33.3%	50.0%	66.7%	100.0%	16.7%	28.6%		28.6%	33.3%	100.0%		
	66.7%	50.0%	33.3%		83.3%	71.4%		66.7%	50.0%			

Figure 18. Data of 80 experiments were used. Confusion chart showing the prediction accuracy of 1D CNN using the FFT, with 50% of the dataset used for training and initial architecture.

Figure 19 content (Accuracy = 63.3333%):

True class \ Predicted class	BASELINE	D1	D2	D3	M1	M2	M3	S1	S2	S3
BASELINE	2		1							
D1		2		1						
D2			2				1			
D3		1		2						
M1				1	1				1	
M2						2	1			
M3						3				
S1								3		
S2								2	1	
S3	1							1		1

Figure 19. Data of 80 experiments were used. Confusion chart showing the prediction accuracy using the STFT spectrograms, with 50% of the dataset used for training and initial architecture.

Accuracy = 50%

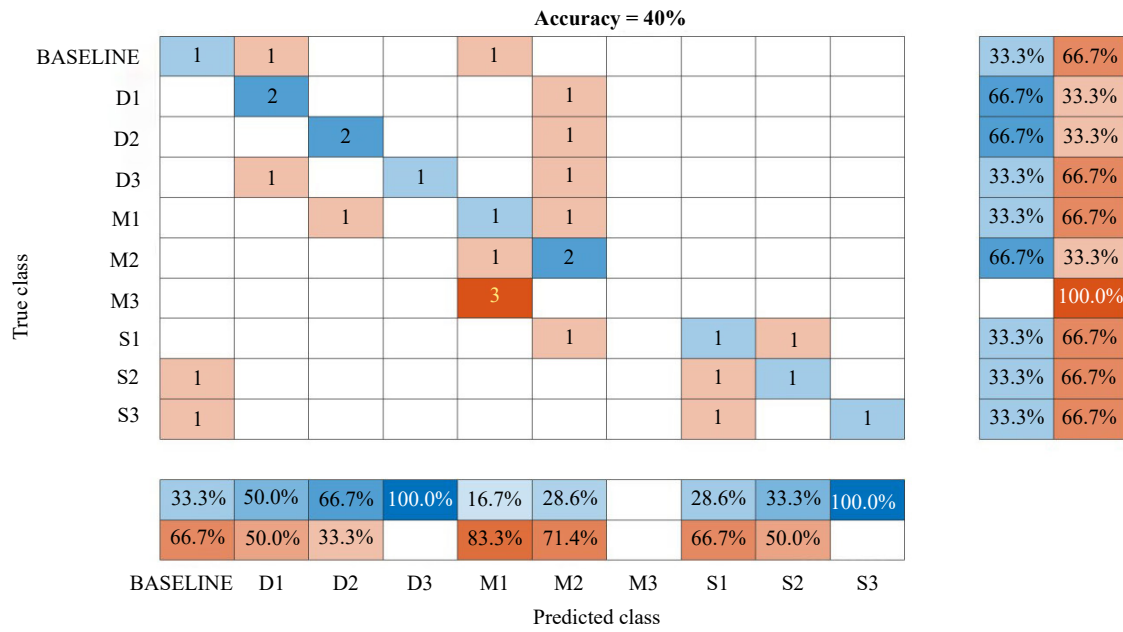| True class \ Predicted	BASELINE	D1	D2	D3	M1	M2	M3	S1	S2	S3
BASELINE	1			1	1					
D1		2	1							
D2			3							
D3		1		2						
M1				1	2					
M2					1	2				
M3				1		2				
S1					1			1		1
S2					1				1	1
S3	2				1					

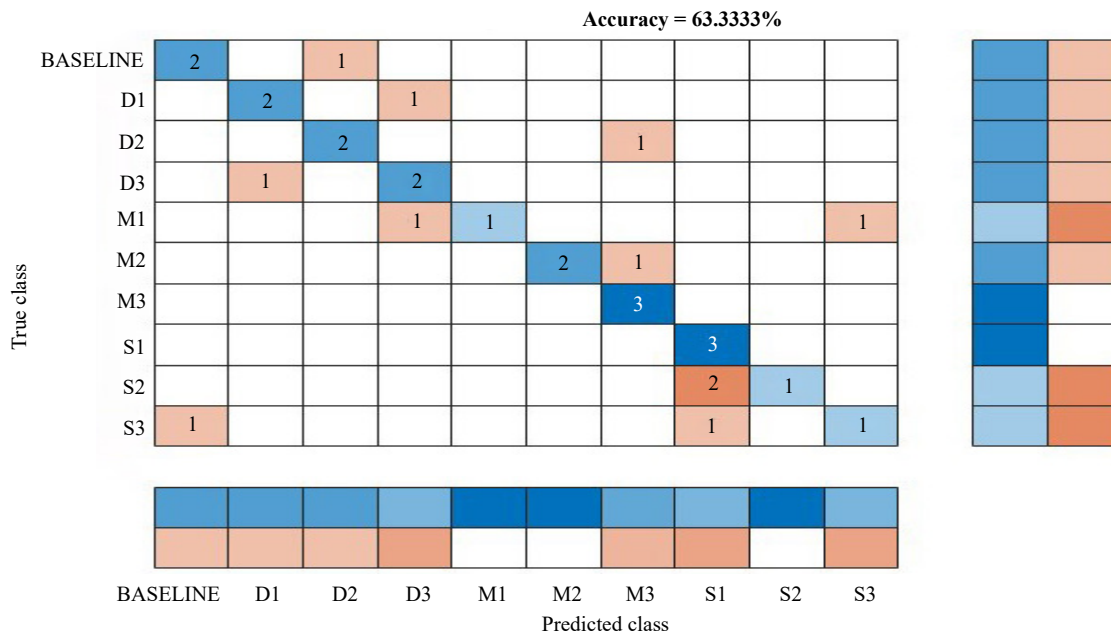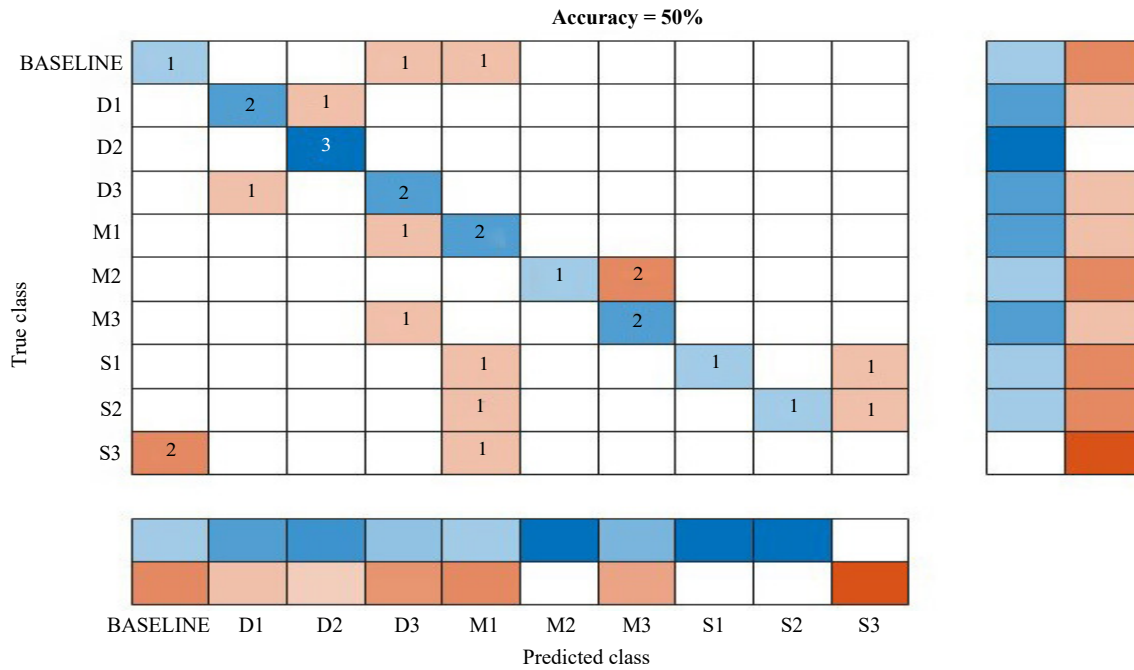Figure 20. Data of 80 experiments were used. Confusion chart showing the prediction accuracy using the CWT scalograms, with 50% of the dataset used for training and initial architecture.

Accuracy = 66.6667%

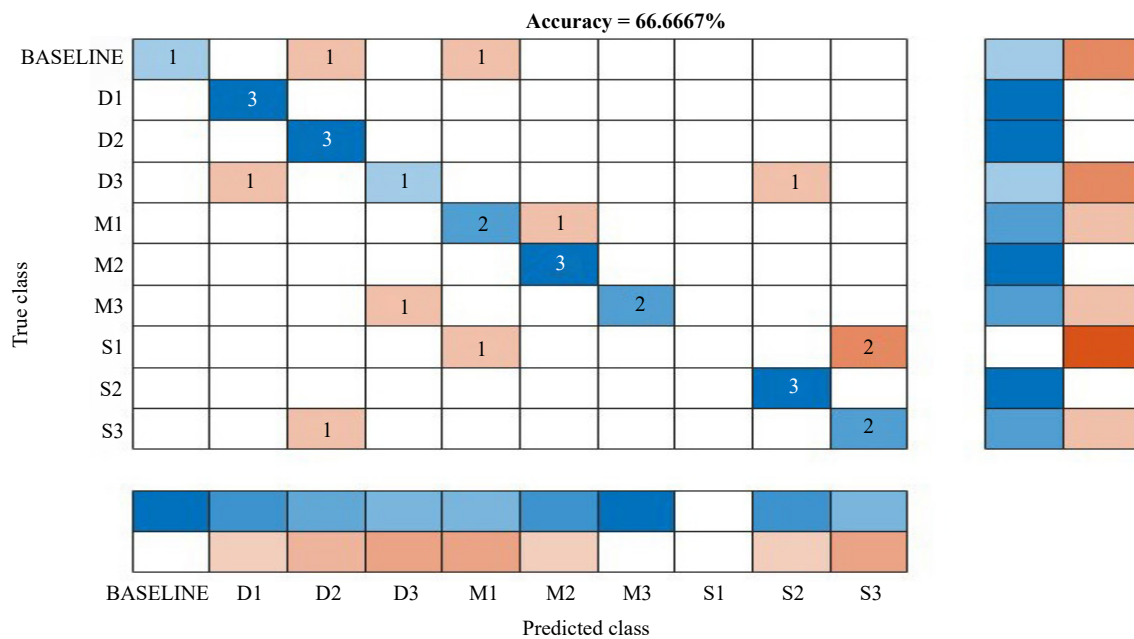| True class \ Predicted	BASELINE	D1	D2	D3	M1	M2	M3	S1	S2	S3
BASELINE	1			1		1				
D1		3								
D2			3							
D3		1		1					1	
M1					2	1				
M2						3				
M3				1			2			
S1					1					2
S2									3	
S3			1							2

Figure 21. Data of 80 experiments were used. Confusion chart showing the prediction accuracy using the SST on CWT scalograms, with 50% of the dataset used for training and initial architecture.

5.4 *Enhancement of the performance of the selected 2D CNN–SST–CWT combination*

After the 2D CNN was selected to work with the SST-enhanced CWT data, test data from 320 experiments were used to evaluate how far the performance of the CWT-SST-2D CNN combination may be improved. The confusion matrix in Figure 22 showed that the performance of the CWT-SST-2D CNN combination increased to 80% accuracy when the data

from 320 tests were used. The accuracy of the same combination was 66% in Figure 21 when 80 datasets were used in the study. 50% of the data was used for training in both studies. The architecture of the 2D CNN was optimized (O2D CNN) with trial and error until the best possible performance was achieved. The new architecture as shown in Figure 8 greatly improved the performance of the CWT-SST-O2D CNN combination to 100% as is seen in Figure 23. 50% of the dataset (images) were used for training. When the training set was further reduced to 30% (96 images), the accuracy remained exceptionally high at 96.36%, as depicted in Figure 24. These results indicate the effectiveness of SST in extracting discriminative features from the data, enabling accurate predictions even with limited training samples.
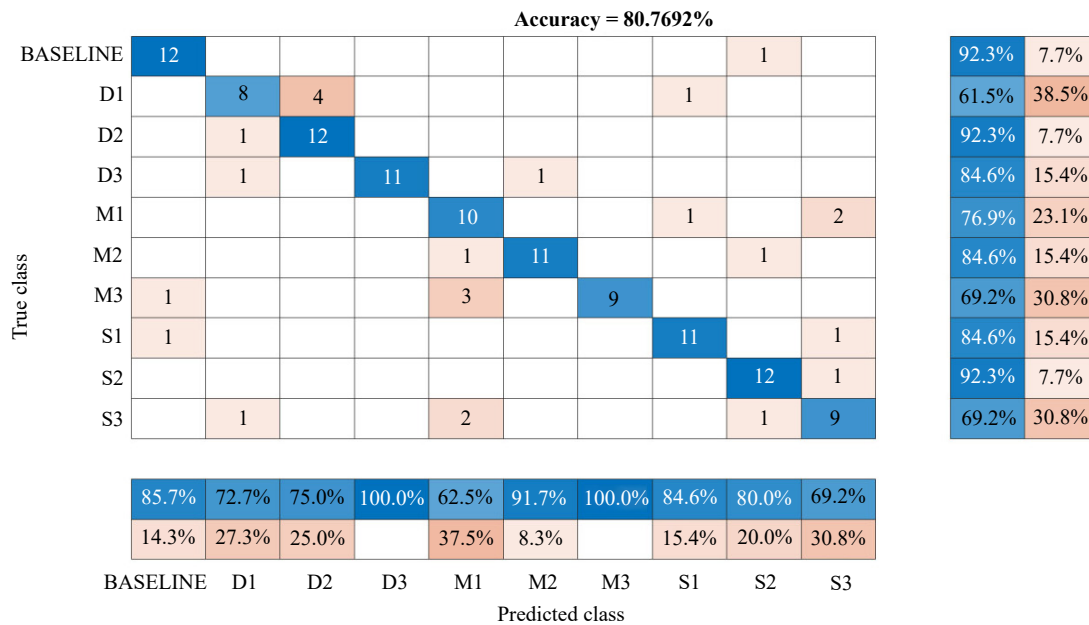
Accuracy = 80.7692%

True class	BASELINE	D1	D2	D3	M1	M2	M3	S1	S2	S3		
BASELINE	12								1		92.3%	7.7%
D1		8	4					1			61.5%	38.5%
D2		1	12								92.3%	7.7%
D3		1		11		1					84.6%	15.4%
M1					10			1		2	76.9%	23.1%
M2					1	11			1		84.6%	15.4%
M3	1				3		9				69.2%	30.8%
S1	1							11		1	84.6%	15.4%
S2									12	1	92.3%	7.7%
S3		1			2				1	9	69.2%	30.8%
	85.7%	72.7%	75.0%	100.0%	62.5%	91.7%	100.0%	84.6%	80.0%	69.2%		
	14.3%	27.3%	25.0%		37.5%	8.3%		15.4%	20.0%	30.8%		
	BASELINE	D1	D2	D3	M1	M2	M3	S1	S2	S3		

Predicted class

Figure 22. Data of 320 experiments were used. Confusion matrix displays a prediction accuracy of 80.77%. This is the result of using 50% of the dataset containing 320 images for training with the initial architecture of the CNN featuring the use of SST on CWT scalograms.
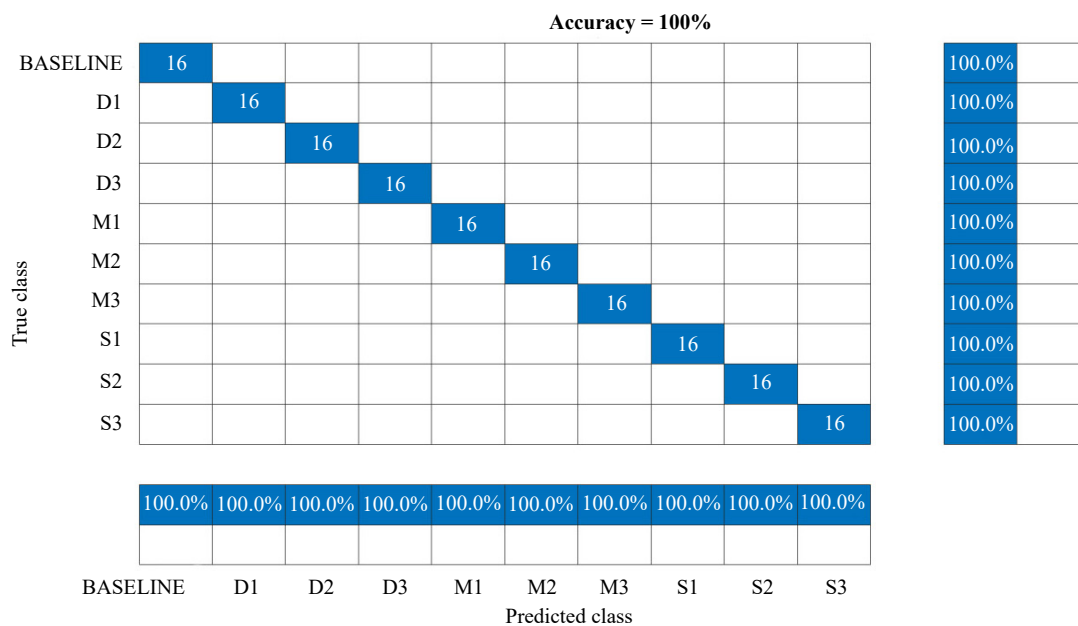
Accuracy = 100%

True class	BASELINE	D1	D2	D3	M1	M2	M3	S1	S2	S3	
BASELINE	16										100.0%
D1		16									100.0%
D2			16								100.0%
D3				16							100.0%
M1					16						100.0%
M2						16					100.0%
M3							16				100.0%
S1								16			100.0%
S2									16		100.0%
S3										16	100.0%
	100.0%	100.0%	100.0%	100.0%	100.0%	100.0%	100.0%	100.0%	100.0%	100.0%	
	BASELINE	D1	D2	D3	M1	M2	M3	S1	S2	S3	

Predicted class

Figure 23. Data of 320 experiments were used. The resulting confusion matrix after the optimization of the CNN architecture. This improved prediction accuracy to 100% while still using 50% of the dataset for training featuring the SST on CWT scalograms.
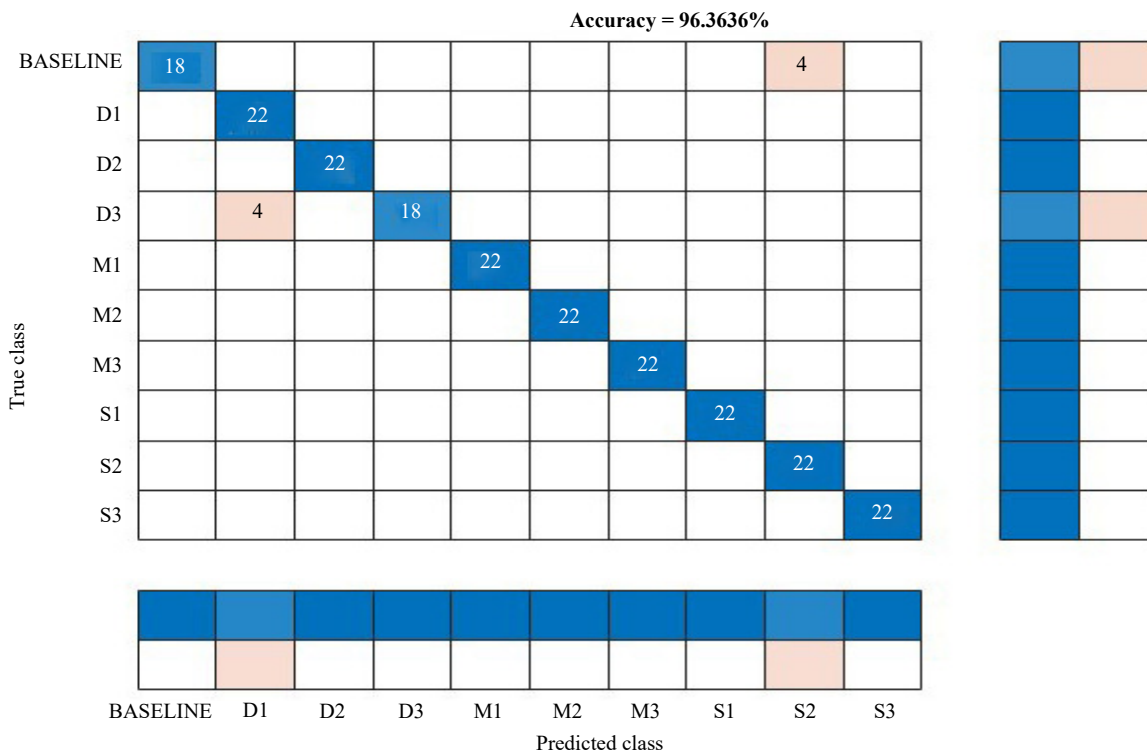
Figure 24. Data of 320 experiments were used. Confusion chart displaying the prediction accuracy using the SST on CWT scalograms, 30% of the dataset was used for training the optimized 2D CNN.

To provide a comprehensive overview of the attained accuracy in each test, Tables 1 and 2 are presented. In Table 1, the performance of the O2D CNN with the improved architecture listed when it worked with the FFT, STFT, CWT, and SST-enhanced CWT. The listed performances in the first row of Table 1 for the optimized 1D and 2D CNNs are better than what were reported in Figures 18 to 21 even though the same number of images were used in both studies. As is seen in the first row of Table 1, 80 images were not enough to exceed 90% accuracy even if the O2D CNN is used. However, the performances of all the combinations immediately improved when the number of the presented cases increased from 80 to 320 in the second row of Table 1, and CWT-SST-O2D CNN obtained 100% accuracy. The results seen in Table 2 prove that at least 160 images are necessary for training the O2D CNN to obtain 100% overall accuracy when there were 320 test cases.

Table 1. Prediction accuracy for both (80 and 320) datasets (spectrum or 2D image), with optimized 2D CNN architecture when the training dataset was 50 % of all data.

Size of dataset	FFT	STFT	CWT	SST on CWT
80	58%	62%	65%	90%
120	93%	95%	94%	100%

Table 2. Prediction accuracy of the 2D CNN with optimized architecture when the training dataset is at different percentages of the overall dataset (images). Data was processed with an SST-CWD combination.

% of dataset used for training	70	60	50	40	30
Prediction accuracy	100%	100%	100%	99.4%	96.3%

6. Conclusions

This study used SHM methods, initially intended for conventionally manufactured parts and structures, for the testing of a metal plate with piezoelectric elements. This research has evaluated the adaptability of these methods to additive manufactured metal parts with complex geometry, particularly a stainless-steel plate with grooves of varying depths. The primary purpose of SHM is to detect and evaluate potential defects. These experiments involved 9 different magnet placements on the plate where LW methods were used to pinpoint defect locations, with data collected using the SuRE method.

Initially, the study started with 80 tests and the standard CNN architecture, resulting in limiting results, with the best performance at 90% using a 2D CNN with a combination of SST and CWT. To improve results, the number of test cases from 80 to 320, and the CNN architecture was optimized, increasing the accuracy to 100%. With the increase in test cases, the FFT-optimized 1D CNN and the STFT-optimized 2D CNN improved accuracy to 93% and 95%, respectively seen in Figure 25 as well.
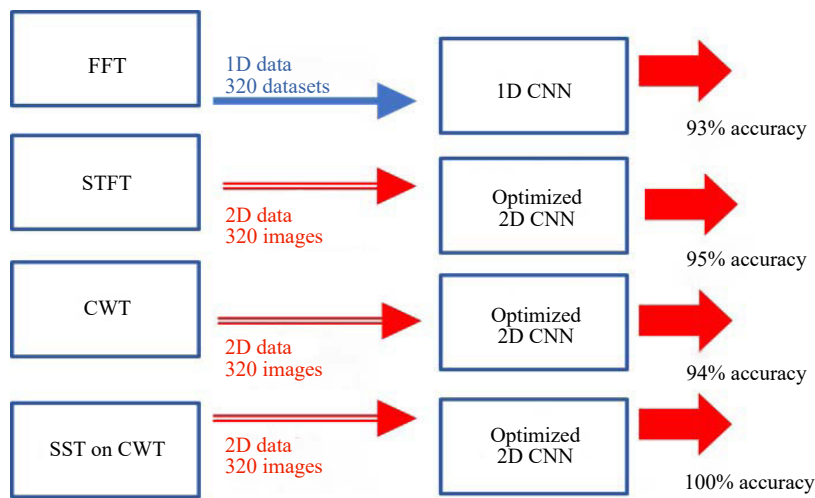

Figure 25. Performance of 1D CNN and 2D CNN when it is used with FFT, STFT, CWT, and SST-CWT signal processing techniques

Four essential requirements were identified to obtain optimal results: a dataset of 160 cases for training, CNN optimization, CWT-SST enhancement for descriptive features, and the presence of grooves with different depths for simplified identification. The study's proposed SHM methods, employing the magnets to simulate various loading conditions and flaws without damaging the part, showed promising results for use in the listed case. Overall, the study successfully demonstrated the potential of SHM methods for additively manufactured metal parts and highlighted important factors for achieving accurate defect identification.

Instead of CNN, future studies may evaluate the performances of other classification methods. The performance of transfer learning may be tested by creating synthetic data and using them as part of the training cases. The performances

of the considered combinations in this study may be evaluated after training with experimental and synthetic data. The experimental procedure may also be changed. Instead of attaching magnets to a test point, this point may be compressed with a vise. Holes may be opened to put bolts at the desired points to create compression. Also, various defects may be simulated by milling the part to collect data at different lengths of a slot. The experiments will be longer, and costlier and preparation of many test parts will be necessary if the part is damaged to see the effect of flaws and performances of the proposed combinations in this study.

Acknowledgments

Conflict of interest

There is no conflict of interest for this study.

References

[1] Zhang Q, Shi Y, Zhao Z. A brief review of mechanical designs for additive manufactured soft materials. *Soft Science*. 2022; 2: 2. https://doi.org/10.20517/ss.2021.22

[2] Giurgiutiu V. *Structural Health Monitoring with Piezoelectric Wafer Active Sensors*. Amsterdam: Elsevier; 2007.

[3] Cawley P. Structural health monitoring: Closing the gap between research and industrial deployment. *Structural Health Monitoring*. 2018; 17(5): 1225-1244. https://doi.org/10.1177/1475921717750047

[4] Su Z, Ye L, Lu Y. Guided lamb waves for identification of damage in composite structures: A review. *Journal of Sound and Vibration*. 2006; 295(3-5): 753-780. https://doi.org/10.1016/j.jsv.2006.01.020

[5] Philibert M, Yao K, Gresil M, Soutis C. Lamb waves-based technologies for structural health monitoring of composite structures for aircraft applications. *European Journal of Materials*. 2022; 2(1): 436-474. https://doi.org/10.1080/26889277.2022.2094839

[6] Annamdas VG, Soh CK. Application of electromechanical impedance technique for engineering structures: review and future issues. *Journal of Intelligent Material Systems and Structures*. 2010; 21(1): 41-59. https://doi.org/10.1177/1045389X09352816

[7] Na WS, Baek J. A review of the piezoelectric electromechanical impedance-based structural health monitoring technique for engineering structures. *Sensors*. 2018; 18(5): 1307. https://doi.org/10.3390/s18051307

[8] Nwokocha F, Hunter D, Zagrai A, Amon D, Cvetic-Thomas D, Weathers D, et al. Electro-mechanical impedance structural health monitoring as an integral component of a flight recorder for space vehicles. *Health Monitoring of Structural and Biological Systems XVI*. 2022; 12048: 154-162. https://doi.org/10.1117/12.2612393

[9] Tansel IN, Singh G, Singh G, Korla S, Grisso BL, Salvino LW, et al. Monitoring the integrity of machine assemblies by using surface response to excitation (SuRE) approach. In: *Proceedings of 5th International Conference on Recent Advances in Space Technologies-RAST2011*. Istanbul, Turkey: IEEE; 2011. p.64-67. https://doi.org/10.1109/RAST.2011.5966917

[10] Tashakori S, Baghalian A, Senyurek VY, Farhangdoust S, McDaniel D, Tansel IN. Composites bond inspection using heterodyne effect and SuRE methods. *Shock and Vibration*. 2018; 2018: 1361932. https://doi.org/10.1155/2018/1361932

[11] Fekrmandi H, Rojas J, Campbell J, Tansel IN, Kaya B, Taskin S. Inspection of the integrity of a multi-bolt robotic arm using a scanning laser vibrometer and implementing the surface response to excitation method (SuRE). *International Journal of Prognostics and Health Management*. 2014; 5(1): 1-10. https://doi.org/10.36001/

ijphm.2014.v5i1.2202

[12] Wang CH, Rose JT, Chang FK. Computerized time-reversal method for structural health monitoring. *Non-destructive Evaluation and Health Monitoring of Aerospace Materials and Composites II*. 2003; 5046: 48-58. https://doi.org/10.1117/12.484668

[13] Tashakori S, Baghalian A, Senyurek VY, Unal M, McDaniel D, Tansel IN. Implementation of heterodyning effect for monitoring the health of adhesively bonded and fastened composite joints. *Applied Ocean Research*. 2018; 72: 51-59. https://doi.org/10.1016/j.apor.2018.01.008

[14] Baghalian A, Tashakori S, Senyurek VY, Unal M, McDaniel D, Tansel IN. Development of comprehensive heterodyne effect-based inspection (CHEBI) method for inclusive monitoring of cracks. *Measurement*. 2018; 128: 89-95. https://doi.org/10.1016/j.measurement.2018.06.030

[15] James JF. *A Student's Guide to Fourier Transforms: with Applications in Physics and Engineering*. 3rd ed. Cambridge: Cambridge University Press; 2011. https://doi.org/10.1017/CBO9780511762307

[16] Finzi Neto RM, Steffen Jr V, Rade DA, Gallo CA, Palomino LV. A low-cost electromechanical impedance-based SHM architecture for multiplexed piezoceramic actuators. *Structural Health Monitoring*. 2011; 10(4): 391-402. https://doi.org/10.1177/1475921710379518

[17] Portnoff M. Time-frequency representation of digital signals and systems based on short-time Fourier analysis. *IEEE Transactions on Acoustics, Speech, and Signal Processing*. 1980; 28(1): 55-69. https://doi.org/10.1109/TASSP.1980.1163359

[18] Strang G. Wavelet transforms versus Fourier transforms. *Bulletin of the American Mathematical Society*. 1993; 28(2): 288-305. https://www.ams.org/journals/bull/1993-28-02/S0273-0979-1993-00390-2/S0273-0979-1993-00390-2.pdf

[19] Tashakori S, Farhangdoust S, Baghalian A, McDaniel D, Tansel IN, Mehrabi A. Damage detection of 3D printed mold using the surface response to excitation method. *Structural Engineering and Mechanics*. 2020; 75(3): 369-376. https://doi.org/10.12989/sem.2020.75.3.369

[20] Tenreiro AF, Lopes AM, da Silva LF. A review of structural health monitoring of bonded structures using electromechanical impedance spectroscopy. *Structural Health Monitoring*. 2022; 21(2): 228-249. https://doi.org/10.1177/1475921721993419

[21] Rumelhart DE, Hinton GE, Williams RJ. Learning representations by back-propagating errors. *Nature*. 1986; 323: 533-536. https://doi.org/10.1038/323533a0

[22] Fekrmandi H, Unal M, Neva SR, Tansel IN, McDaniel D. A novel approach for classification of loads on plate structures using artificial neural networks. *Measurement*. 2016; 82: 37-45. https://doi.org/10.1016/j.measurement.2015.12.027

[23] Lopes Jr V, Park G, Cudney HH, Inman DJ. Impedance-based structural health monitoring with artificial neural networks. *Journal of Intelligent Material Systems and Structures*. 2000; 11(3): 206-214. https://doi.org/10.1106/H0EV-7PWM-QYHW-E7VF

[24] Lee JW, Kirikera GR, Kang I, Schulz MJ, Shanov VN. Structural health monitoring using continuous sensors and neural network analysis. *Smart Materials and Structures*. 2006; 15(5): 1266. https://doi.org/10.1088/0964-1726/15/5/016

[25] Widodo A, Yang BS. Support vector machine in machine condition monitoring and fault diagnosis. *Mechanical Systems and Signal Processing*. 2007; 21(6): 2560-2574. https://doi.org/10.1016/j.ymssp.2006.12.007

[26] Satpal SB, Khandare Y, Guha A, Banerjee S. Structural health monitoring of a cantilever beam using support vector machine. *International Journal of Advanced Structural Engineering*. 2013; 5: 2. https://doi.org/10.1186/2008-6695-5-2

[27] Miorelli R, Kulakovskyi A, Chapuis B, D'almeida O, Mesnil O. Supervised learning strategy for classification and regression tasks applied to aeronautical structural health monitoring problems. *Ultrasonics*. 2021; 113: 106372. https://doi.org/10.1016/j.ultras.2021.106372

[28] Vitola J, Pozo F, Tibaduiza DA, Anaya M. A sensor data fusion system based on *k*-nearest neighbour pattern classification for structural health monitoring applications. *Sensors*. 2017; 17(2): 417. https://doi.org/10.3390/s17020417

[29] Cover T, Hart P. Nearest neighbor pattern classification. *IEEE Transactions on Information Theory*. 1967; 13(1):

21-27. https://doi.org/10.1109/TIT.1967.1053964

[30] Kurian B, Liyanapathirana R. Machine learning techniques for structural health monitoring. In: Wahab M. (ed.) *Proceedings of the 13th International Conference on Damage Assessment of Structures*. Lecture Notes in Mechanical Engineering. Singapore: Springer; 2020. p.3-24. https://doi.org/10.1007/978-981-13-8331-1_1

[31] Ewald V, Groves RM, Benedictus R. DeepSHM: A deep learning approach for structural health monitoring based on guided Lamb wave technique. *Sensors and Smart Structures Technologies for Civil, Mechanical, and Aerospace Systems*. 2019; 10970: 84-99. https://doi.org/10.1117/12.2506794

[32] Modir A, Tansel I. Structural health monitoring of additively manufactured parts by combining infill design, multiple pulse width excitation (MPWE), and deep learning. *Journal of Vibration Engineering & Technologies*. 2022; 10(8): 3227-3238. https://doi.org/10.1007/s42417-022-00553-5

[33] De Oliveira MA, Monteiro AV, Vieira Filho J. A new structural health monitoring strategy based on PZT sensors and convolutional neural network. *Sensors*. 2018; 18(9): 2955. https://doi.org/10.3390/s18092955

[34] Hull CW. *Apparatus for Production of Three-Dimensional Objects by Stereolithography*. US4575330A (Patent) 1984.

[35] Crump SS. *Apparatus and Method for Creating Three-Dimensional Objects*. US5121329A (Patent) 1992.

[36] Deckard CR. *Method and Apparatus for Producing Parts by Selective Sintering*, US4863538A (Patent) 1989.

[37] Bremen S, Meiners W, Diatlov A. Selective laser melting: A manufacturing technology for the future? *Laser Technik Journal*. 2012; 9(2): 33-38. https://doi.org/10.1002/latj.201290018

[38] Roshchupkin S, Kolesov A, Tarakhovskiy A, Tishchenko I. A brief review of main ideas of metal fused filament fabrication. Materials *Today: Proceedings*. 2021; 38: 2063-2067. https://doi.org/10.1016/j.matpr.2020.10.142

[39] Singh S, Sharma SK, Rathod DW. A review of process planning strategies and challenges of WAAM. *Materials Today: Proceedings*. 2021; 47: 6564-6575. https://doi.org/10.1016/j.matpr.2021.02.632

[40] Kumar P, Singh RK, Sharma SK. Effect of welding parameters on bead characteristics and mechanical properties of wire and arc additive manufactured inconel 718. *Proceedings of the Institution of Mechanical Engineers, Part C: Journal of Mechanical Engineering Science*. 2022; 237(7): 1668-1691. https://doi.org/10.1177/09544062221133035

[41] Ralph B. *Method of Making Decorative Articles*. US1533300A (Patent) 1925.

[42] Attaran M. The rise of 3-D printing: The advantages of additive manufacturing over traditional manufacturing. Business Horizons. 2017; 60(5): 677-688. https://doi.org/10.1016/j.bushor.2017.05.011

[43] Mehrpouya M, Dehghanghadikolaei A, Fotovvati B, Vosooghnia A, Emamian SS, Gisario A. The potential of additive manufacturing in the smart factory industrial 4.0: A review. *Applied Sciences*. 2019; 9(18): 3865. https://doi.org/10.3390/app9183865

[44] Mohamed AF, Shah KY, Tansel IN. Compressive force location estimation with SuRE method for additively manufactured parts. *Procedia Manufacturing*. 2019; 39: 465-473. https://doi.org/10.1016/j.promfg.2020.01.403

[45] Lim YY, Smith ST, Soh CK. Wave propagation-based monitoring of concrete curing using piezoelectric materials: Review and path forward. *NDT & E International*. 2018; 99: 50-63. https://doi.org/10.1016/j.ndteint.2018.06.002

[46] Ulriksson B. Conversion of frequency-domain data to the time domain. *Proceedings of the IEEE*. 1986; 74(1): 74-77. https://doi.org/10.1109/PROC.1986.13405

[47] Mopsik FI. The transformation of time-domain relaxation data into the frequency domain. *IEEE Transactions on Electrical Insulation*. 1985: EI-20(6): 957-964. https://doi.org/10.1109/TEI.1985.348736

[48] Kiymik MK, Güler İ, Dizibüyük A, Akın M. Comparison of STFT and wavelet transform methods in determining epileptic seizure activity in EEG signals for real-time application. *Computers in Biology and Medicine*. 2005; 35(7): 603-616. https://doi.org/10.1016/j.compbiomed.2004.05.001

[49] Alsberg BK, Woodward AM, Kell DB. An introduction to wavelet transforms for chemometricians: A time-frequency approach. *Chemometrics and Intelligent Laboratory Systems*. 1997; 37(2): 215-239. https://doi.org/10.1016/S0169-7439(97)00029-4

[50] Staszewski WJ, Boller C, Tomlinson GR. *Health Monitoring of Aerospace Structures: Smart Sensor Technologies and Signal Processing*. Chichester, England: Wiley; 2004. https://doi.org/10.1002/0470092866

[51] Sorensen HV, Burrus CS. Efficient computation of the short-time fast Fourier transform. In: *ICASSP-88., International Conference on Acoustics, Speech, and Signal Processing*. New York, USA: IEEE Computer Society;

1988. p.1894-1897. https://doi.ieeecomputersociety.org/10.1109/ICASSP.1988.196996

[52] Kehtarnavaz Nasser. *Digital Signal Processing System Design LabVIEW-based Hybrid Programming*. 2nd ed. USA: Academic Press; 2008. https://doi.org/10.1016/B978-0-12-374490-6.X0001-3

[53] Sifuzzaman M, Islam MR, Ali MZ. Application of wavelet transform and its advantages compared to Fourier transform. *Journal of Physical Science*. 2009; 13: 121-134. https://citeseerx.ist.psu.edu/document?repid=rep1&type=pdf&doi=63f422a5095dd2e4e190ce7f589cab75232402f1

[54] Guo T, Zhang T, Lim E, Lopez-Benitez M, Ma F, Yu L. A review of wavelet analysis and its applications: Challenges and opportunities. *IEEE Access*. 2022; 10: 58869-58903. https://doi.org/10.1109/ACCESS.2022.3179517

[55] Zhao C, He M, Zhao X. Analysis of a transient waveform based on combined short-time Fourier transform and wavelet transform. In: *2004 International Conference on Power System Technology, PowerCon 2004*. Singapore: IEEE; 2004. p.1122-1126. https://doi.org/10.1109/ICPST.2004.1460169

[56] Daubechies I. *Ten Lectures on Wavelets*. CBMS-NSF Regional Conference Series in Applied Mathematics. Pennsylvania: Society for Industrial and Applied Mathematics; 1992. https://doi.org/10.1137/1.9781611970104

[57] Zhang D. Wavelet transform. In: *Fundamentals of image data mining*. Texts in Computer Science. Cham: Springer; 2019. p. 35-44. https://doi.org/10.1007/978-3-030-17989-2_3

[58] Shuman DI, Ricaud B, Vandergheynst P. A windowed graph Fourier transform. *2012 IEEE Statistical Signal Processing Workshop (SSP)*. Ann Arbor, MI, USA: IEEE; 2012. p.133-136. https://doi.org/10.1109/SSP.2012.6319640

[59] Taha MR, Noureldin A, Lucero JL, Baca TJ. Wavelet transform for structural health monitoring: A compendium of uses and features. *Structural Health Monitoring*. 2006; 5(3): 267-295. https://doi.org/10.1177/1475921706067741

[60] Robertson DC, Camps OI, Mayer JS, Gish WB. Wavelets and electromagnetic power system transients. *IEEE Transactions on Power Delivery*. 1996; 11(2): 1050-1058. https://doi.org/10.1109/61.489367

[61] Conraria LA, Soares MJ. *The continuous wavelet transforms: A primer*. Braga: Núcleo de Investigação em Políticas Económicas (NIPE); 2010. https://hdl.handle.net/1822/11707

[62] Thakral S, Manhas P. Image processing by using different types of discrete wavelet transform. In: Luhach A, Singh D, Hsiung PA, Hawari K, Lingras P, Singh P. (eds.) *Advanced Informatics for Computing Research. ICAICR 2018*. Communications in Computer and Information Science, vol 955. Singapore: Springer; 2019. p.499-507. https://doi.org/10.1007/978-981-13-3140-4_45

[63] Ghazali KH, Mansor MF, Mustafa MM, Hussain A. Feature extraction technique using discrete wavelet transform for image classification. In: *2007 5th Student Conference on Research and Development*. Selangor, Malaysia: IEEE; 2007. p.1-4. https://doi.org/10.1109/SCORED.2007.4451366

[64] Meignen S, Oberlin T, Pham DH. Synchrosqueezing transforms: From low-to high-frequency modulations and perspectives. *Comptes Rendus Physique*. 2019; 20(5): 449-460. https://doi.org/10.1016/j.crhy.2019.07.001

[65] Huang ZL, Zhang J, Zhao TH, Sun Y. Synchrosqueezing S-transform and its application in seismic spectral decomposition. *IEEE Transactions on Geoscience and Remote Sensing*. 2016; 54(2): 817-825. https://doi.org/10.1109/TGRS.2015.2466660

[66] He D, Cao H, Wang S, Chen X. Time-reassigned synchrosqueezing transform: The algorithm and its applications in mechanical signal processing. *Mechanical Systems and Signal Processing*. 2019; 117: 255-279. https://doi.org/10.1016/j.ymssp.2018.08.004

[67] O'Shea K, Nash R. An introduction to convolutional neural networks. *ArXiv* [Preprint] 2015. Version 2. https://arxiv.org/abs/1511.08458v2

[68] National Instruments. *Understanding FFTs and Windowing*. https://download.ni.com/evaluation/pxi/Understanding%20FFTs%20and%20Windowing.pdf [Accessed 7th February 2023].

[69] Rose WC. *Mathematics and Signal Processing for Biomechanics*. https://www1.udel.edu/biology/rosewc/kaap686/notes/windowing [Accessed 7th February 2023].

[70] Achenbach JD. Quantitative non-destructive evaluation. *International Journal of Solids and Structures*. 2000; 37(1-2): 13-27. https://doi.org/10.1016/S0020-7683(99)00074-8

[71] Tibaduiza Burgos DA, Gomez Vargas RC, Pedraza C, Agis D, Pozo F. Damage identification in structural health monitoring: A brief review from its implementation to the use of data-driven applications. *Sensors*. 2020; 20(3):

733. https://doi.org/10.3390/s20030733

[72] Yuan FG. (ed.) *Structural Health Monitoring (SHM) in Aerospace Structures*. Duxford, UK: Woodhead Publishing; 2016. https://doi.org/10.1016/C2014-0-00994-X

[73] Doebling SW, Farrar CR, Prime MB, Shevitz DW. *Damage identification and health monitoring of structural and mechanical systems from changes in their vibration characteristics: A literature review*. Los Alamos National Lab. (LANL). Report Number: LA-13070-MS, 1996. https://doi.org/10.2172/249299

[74] Fan G, Li J, Hao H. Dynamic response reconstruction for structural health monitoring using densely connected convolutional networks. *Structural Health Monitoring*. 2021; 20(4): 1373-1391. https://doi.org/10.1177/1475921720916881

[75] Gopalakrishnan S, Ruzzene M, Hanagud S. *Computational techniques for structural health monitoring*. London: Springer; 2011. https://doi.org/10.1007/978-0-85729-284-1

[76] Gul M, Catbas FN. Structural health monitoring and damage assessment using a novel time series analysis methodology with sensor clustering. *Journal of Sound and Vibration*. 2011; 330(6): 1196-1210. https://doi.org/10.1016/j.jsv.2010.09.024

[77] Ling Y, Mahadevan S. Integration of structural health monitoring and fatigue damage prognosis. *Mechanical Systems and Signal Processing*. 2012; 28: 89-104. https://doi.org/10.1016/j.ymssp.2011.10.001

[78] Modir Alireza, Shah KY, Mohamed AF, Tansel IN. Additively manufactured multi-material parts with defect detection capabilities. *Procedia Manufacturing*. 2019; 39: 493-501. https://doi.org/10.1016/j.promfg.2020.01.406

[79] Nasrollahi A, Deng W, Ma Z, Rizzo P. Multimodal structural health monitoring based on active and passive sensing. *Structural Health Monitoring*. 2017; 17(2): 395-409. https://doi.org/10.1177/1475921717699375

[80] Park G, Farrar CR, di Scalea FL, Coccia S. Performance assessment and validation of piezoelectric active-sensors in structural health monitoring. *Smart Materials and Structures*. 2006; 15(6): 1673. https://doi.org/10.1088/0964-1726/15/6/020

[81] Worden K, Dulieu-Barton JM. An overview of intelligent fault detection in systems and structures. *Structural Health Monitoring*. 2004; 3(1): 85-98. https://doi.org/10.1177/1475921704041866

[82] Yuan FG, Zargar SA, Chen Q, Wang S. Machine learning for structural health monitoring: challenges and opportunities. *Sensors and Smart Structures Technologies for Civil, Mechanical, and Aerospace Systems*. 2020; 11379: 1137903. https://doi.org/10.1117/12.2561610

[83] Blakey-Milner B, Gradl P, Snedden G, Brooks M, Pitot J, Lopez E, et al. Metal additive manufacturing in aerospace: A review. *Materials and Design*. 2021; 209: 110008. https://doi.org/10.1016/j.matdes.2021.110008